RSC Advances

PAPER

View Article Online
View Journal | View Issue

Cite this: *RSC Adv.*, 2026, **16**, 28955

A novel strategy for the photothermal treatment and electroencephalogram monitoring of *in situ* glioma

Haoyang Zhang,†[a] Ke Shi,†[a] Wenxuan Zhang,[c] Xue Chen,[c] Xi Wang,[b] Yan Zhao,[a] Hengyuan Pang,[a] Xi Chen*[b] and Jianjiao Wang *[a]

The current photothermal treatments for glioma suffer from inappropriate tumor models, nanoparticle-related long-term intracranial retention, and the absence of real-time electroencephalography monitoring. Herein, we report the development of an integrated photothermal therapy (PTT)-electroencephalogram (EEG) monitoring system based on micropyramid-structured polypyrrole (*m*-PPy) film patches, enabling the accurate and controllable treatment of intracranial gliomas *in situ* while providing the real-time monitoring of intraoperative complications. The pyramid architecture of the *m*-PPy film endows it with excellent photothermal conversion efficiency and electrochemical behavior, which allow it to simultaneously function as a photothermal agent for tumor ablation and a bioelectrode for electroencephalography signal collection. The flexible and stretchable nature of *m*-PPy allows it to adhere well to tumors for preventing glioma rupture while obtaining stable signal acquisition. More importantly, it can be completely removed after surgery to prevent the long-term toxicity caused by intracranial residues. *In vitro* experiments suggest that it induces C6 glioma cell apoptosis through the upregulation of Anxa5 and Csrp3 coupled with the downregulation of septin-4, effectively activating the apoptotic pathway. In orthotopic tumor models, the integrated system achieves complete tumor ablation while simultaneously monitoring intraoperative neuroelectrophysiological changes in real-time through EEG (*via* the dynamic analysis of the $\alpha/\theta/\beta$ wave power spectra), achieving a temperature control accuracy of ± 0.8 °C mm^{-1}. Proteomic analysis revealed that PTT significantly inhibits tumor migration by suppressing mitochondrial complex I (as evidenced by the downregulation of NDUFB2/4) and motor protein pathways. Hence, this platform overcomes critical barriers in glioma therapy by eliminating invasive procedures while ensuring the real-time detection of treatment complications.

Received 20th January 2026
Accepted 31st March 2026

DOI: 10.1039/d6ra00499g

rsc.li/rsc-advances

1 Introduction

Gliomas are the most aggressive primary tumors of the central nervous system, and their treatment remains a significant challenge in neuro-oncology. The median survival time for patients with WHO Grade IV glioblastoma multiforme (GBM) is only 12–15 months, and the five-year survival rate is less than 5%.[1–3] Current treatment modalities, including surgical resection, radiation therapy, and chemotherapy, have limitations towards curing gliomas. The efficacy of surgical intervention is constrained by the functional protection requirements of neuroanatomy. Although intraoperative neuro-navigation and fluorescence guidance techniques (such as 5-ALA) have improved tumor identification accuracy,[4] invasive tumor cells in functional cortical areas (such as language centers and motor regions) are difficult to remove completely. Even when the "total resection" criteria are met, postoperative MRI enhancement scans still detect more than 10^6 residual tumor cells.[5] Radiotherapy also has limitations. Glioma stem cells (GSCs) exhibit strong radio-resistance, which is closely related to their DNA repair activation and hypoxic microenvironment.[6,7] Clinical data indicate that standard radiotherapy regimens (60 Gy/30 fractions) can only increase local control rates by about 30%.[8] Chemotherapy towards glioma treatment suffers from inefficient drug delivery across the blood–brain barrier (BBB). Even for the high-grade glioma chemotherapy drug temozolomide (TMZ), its cerebrospinal fluid/plasma concentration ratio is only 0.2–0.3.[9,10] More critically, the overexpression of drug efflux pumps (such as *P*-glycoprotein) due to glioma heterogeneity can reduce the drug concentration in tumor tissues by more than 10 times compared with the surrounding brain tissues.[11] This dual barrier effect not only leads to treatment failure but also triggers

[a]*Department of Neurosurgery, Second Affiliated Hospital of Harbin Medical University, Harbin, 150086, P. R. China. E-mail: wangjianjiao@163.com*

[b]*Department of Breast, Second Affiliated Hospital of Harbin Medical University, Harbin, 150086, P. R. China*

[c]*Oral Department, Second Affiliated Hospital of Harbin Medical University, Harbin, 150086, P. R. China*

† Haoyang Zhang and Ke Shi contributed equally to this work.

severe complications such as bone marrow suppression due to systemic toxicity. These therapeutic bottlenecks at the molecular level reflect the evolutionary characteristics of gliomas; for example, the infiltrative growth pattern evades local treatment, genetic heterogeneity weakens targeted therapy efficacy, and an immunosuppressive microenvironment hinders sustained control.[12] Therefore, developing new therapeutic modalities that can overcome anatomical barriers and achieve precise energy delivery has become a key scientific challenge for improving treatment outcomes.

In the past decade, photothermal therapy (PTT) has emerged as a revolutionary approach to address the challenges of cancer treatment.[13,14] It relies on localized photothermal agents (PTAs) to convert light energy into hyperthermia under near-infrared (NIR, 700–1100 nm) irradiation, thereby destroying tumors.[15,16] The therapeutic specificity of PTT stems from two distinct biophysical advantages: (1) the activation of PTT is strictly controlled by the co-localization of PTAs and NIR, ensuring spatial accuracy, and (2) the light absorption efficiency of photothermal agents is fundamentally governed by their structural characteristics. Multiscale structural synergies, such as periodic micro-/nano-architectures (*e.g.*, pyramids, inverted pyramids, nanowires, and nanopores), can dramatically alter light propagation pathways through multiple reflections and impedance matching. Surface roughness further promotes intense light scattering or localized surface plasmon resonance, while near-field optical enhancement effects can amplify absorption at the nanoscale. Collectively, these structural factors dictate the overall photothermal conversion performance.[17–19] Meanwhile, glioma cells are more sensitive to thermal damage compared to normal neurons, with a critical thermal tolerance threshold (42–45 °C) lower than that of neural tissue (which can tolerate 48 °C for 5 minutes).[20,21] PTT has unique advantages in the treatment of intracranial tumors. Firstly, NIR can penetrate brain tissue to a depth of 3–5 cm, effectively covering deep-seated lesions.[22] Secondly, the relatively homogeneous structure of brain tissue can reduce light scattering, enabling millimeter-level spatial precision when combined with a neuro-navigation system.[23] Thirdly, thermal-induced tumor vascular occlusion can block peripheral invasion pathways, generating a "distant effect" beyond the direct thermal ablation range.[24] These characteristics make PTT an ideal choice for treating intracranial tumors and enable it to overcome the limitations of traditional treatment methods.

However, there are three scientific bottlenecks in the current PTT research towards glioma. The first bottleneck concerns the tumor model. Previous studies predominantly relied on subcutaneous xenograft models,[25,26] which have the following limitations. (1) A lack of brain-specific vascular structure; the permeability of the blood-tumor barrier (BTB) (~8 nm) is significantly higher than that of the blood–brain barrier (4–6 nm),[27] leading to an overestimation of PTA transport and biological behavior. (2) Immune microenvironment differences; subcutaneous models lack microglial infiltration and cerebrospinal fluid circulation, failing to simulate the immunosuppressive features of gliomas.[28] (3) Metabolic environment differences; the high lactate concentration (2–5 mM) unique to brain tissue significantly affects the surface charge and aggregation state of PTA.[29] These factors result in a significant discrepancy between the therapeutic response of subcutaneous models and the actual efficacy in the cranium. Secondly, nanoparticle-mediated PTT is not suitable for intracranial applicability.[30] Nanoparticles are easily blocked by the tight junctions of BBB endothelial cells (gap < 20 nm), and osmotic agents are required to open the barrier, potentially inducing cerebral edema.[31] Moreover, the half-life of nanoparticles in brain tissue exceeds 30 days, and long-term retention may trigger microglial activation and the release of pro-inflammatory factors (IL-1β and TNF-α), exacerbating neuroinflammation.[32] The incomplete metabolism also leads to the generation of reactive oxygen species (ROS), causing neuronal mitochondrial DNA damage.[33] Thirdly, the PTT research in glioma lacks a neuro-safety monitoring system, failing to address sudden pathological events that may occur during treatment, such as hemodynamic disturbances, metabolic crisis, autonomic nervous dysfunction, and so forth. The current PTT lacks integrated electrophysiological monitoring modules, which are essential for early warning of intraoperative complications and achieving a 'treatment-feedback' control.

To address the aforementioned scientific bottlenecks, this study has (1) established an *in situ* glioma model that retains the characteristics of the brain microenvironment, (2) developed a polypyrrole (PPy) photothermal patch with an excellent interface compatibility for PTT treatment, which also (3) serves as a bioelectrode for integration with a multi-channel electroencephalography (EEG) real-time monitoring system. Specifically, an *in situ* glioma model was established by stereotaxically injecting C6 cells into the right striatum of nude mice.[34] This model fully preserves the three-dimensional infiltration characteristics of brain tissue and the dynamic evolution process of the blood–brain barrier (BTB). To address the shortcomings of the intracranial retention problem in traditional nanoparticle-based PTT, we designed a PPy film patch (5 ± 2 μm thick), which can cover the surface of the tumor to form a conformal interface. The PPy film patch functions as both a photothermal layer and a bioelectrode. It can achieve precise temperature control under irradiation and also combine with a real-time EEG detection system to ensure intraoperative safety monitoring. If the power spectral density of the γ band increases by more than 40% (indicating an increase in blood pressure), or the δ wave ratio remains above 60% (indicating insufficient cerebral perfusion), the system will trigger an alarm. At this point, external medical interventions, such as the infusion of antihypertensive drugs or oxygen therapy, can be promptly initiated to address any sudden issues. We also elucidated the molecular mechanisms of PTT-induced glioma inhibition through proteomics analysis. The upregulation of tumor migration-related proteins (such as Anxa5, CSRP3) and the significant downregulation of cytoskeletal remodeling factors (such as Septin-4) indicate that hyperthermia disrupts the stability of adhesion complexes and microtubule networks, thereby impairing the motility and invasiveness of glioma cells (Scheme 1). These findings not only validate the therapeutic potential of PPy but also provide mechanistic insights into the

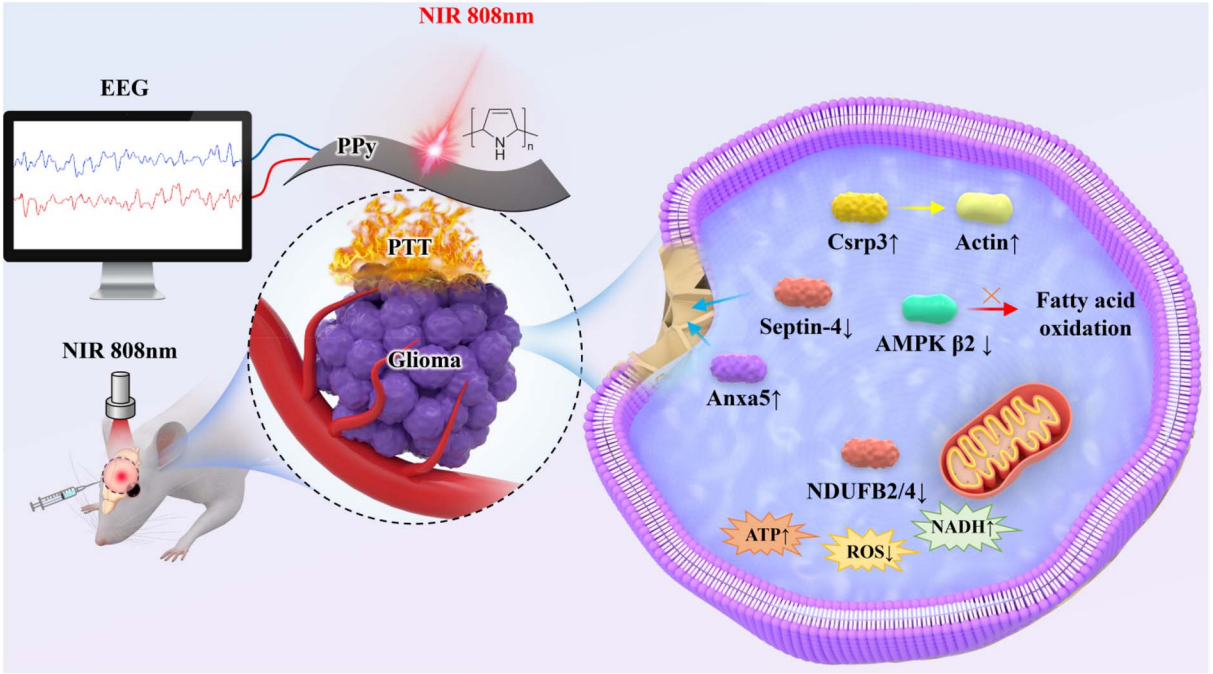

Scheme 1 Schematic of the *m*-PPy-mediated photothermal therapy combined with intraoperative electroencephalogram monitoring.

anti-metastatic effects of PTT. In summary, this study has achieved glioma treatment from "blind thermal ablation" to "visible and controllable" through innovative material design, tumor model optimization and monitoring technology.

2 Materials and methods

2.1 Materials

Single-sided polished silicon wafers were purchased from CW-Nano, Shanghai, China. Phosphate buffer and 1640 medium were purchased from Sigma-Aldrich, Shanghai, China. Pyrrole (Py), propidium iodide (PI, ≥94%), and calcein acetoxymethyl ester (calcein-am, ≥96%) were purchased from Aladdin, Shanghai, China. *P*-toluenesulfonic acid (PTSA) was purchased from McLean Biochemical Company, Shanghai, China. Penicillin-streptomycin and fetal bovine serum (FBS) were purchased from Gibco Life Technologies (Shanghai, China). 3-(4,5-Dimethylthiazol-2-yl)-2,5-diphenyltetrazolium bromide (MTT, 98%) was purchased from Solarbio Technology Ltd (Beijing, China). PBS and trypsin were purchased from HyClone (China).

2.2 Synthesis of PPy

Micropyramid-structured silicon wafers were prepared by isotropic etching in KOH/isopropanol solution, a method previously established for fabricating textured silicon surfaces. The P100-oriented silicon wafers were initially sectioned into 2 cm × 3 cm rectangles and underwent a cleaning process involving immersion in an acetone and ethanol solution under ultrasonication to ensure surface purity. Subsequently, a solution comprising 5.5 g KOH, 25 mL isopropanol and 100 mL water was prepared. The silicon wafer was then immersed in this solution and subjected to isotropic etching at 60 °C for 70 min to induce a micropyramid structure on the surface.[35–37] The planar PPy film (*p*-PPy) was prepared by electrochemical deposition on ITO conductive glass (working electrode) in an electrolyte solution containing 0.5 g pyrrole monomer and 2 g *p*-toluenesulfonic acid (PTSA) in 100 mL deionized water at 0 °C. The electrochemical deposition was performed using a three-electrode system with a platinum sheet as the counter electrode and Ag/AgCl as the reference electrode. The deposition was carried out at a constant current density of 1 mA cm^{-2} for 30 min at 0 °C, following previously reported methods.[38,39] Additionally, the micropyramidal PPy film (*m*-PPy) was prepared on silicon wafers etched with a micro-pyramidal structure (working electrode) under identical electrochemical conditions. Each experiment was conducted in triplicate to ensure the reproducibility of the results.

2.3 Evaluation of electrochemical and photothermal performances

The influence of the molar ratios of pyrrole monomer (Py) to *p*-toluenesulfonic acid (PTSA) (0.5 : 1, 1 : 1, 2 : 1, and 3 : 1) on the conductivity of the films was investigated using a four-probe measurement system (Jandel RM3000) at room temperature. The optical absorbance of the films was recorded on a UV-Vis spectrophotometer (Shimadzu UV-3600) over a wavelength range of 300–1200 nm. To assess the photothermal stability of the films, five on/off cycles were performed with an 808 nm NIR laser (0.3 W cm^{-2}, 10 min irradiation per cycle), and the thermal response was recorded using an infrared thermal imaging camera. The electrochemical characteristics of *p*-PPy and *m*-PPy

films were studied using an electrochemical workstation (CHI660E, CH Instruments). A three-electrode system was employed: *p*-PPy and *m*-PPy films, Ag/AgCl electrode and a platinum sheet were used as the working electrode, reference electrode and counter electrode, respectively, in 0.1 M PBS (pH 7.4) electrolyte. Electrochemical impedance spectroscopy (EIS, frequency range 0.1 Hz to 100 kHz) was conducted in the frequency range of 0.1 Hz to 100 kHz with an AC amplitude of 5 mV, and cyclic voltammetry (CV) measurements were performed at a scan rate of 100 mV s^{-1} within a potential range of −0.2 to 0.8 V. The stability and resistance to biomolecular interference of the films were evaluated using chronoamperometry (*I–T* curves) under a constant voltage of 0.6 V in PBS before and after the addition of 1 mM ascorbic acid.

2.4 Cell culture and *in vitro* cytotoxicity measurements

C6 rat glioma cells (obtained from the Cell Bank of the Chinese Academy of Sciences) were cultured in RPMI-1640 medium (Gibco) supplemented with 10% (v/v) fetal bovine serum (FBS, Gibco) and 1% penicillin-streptomycin (100 U mL^{-1}, HyClone) at 37 °C in an incubator with 5% CO_2. For cytotoxicity assays, C6 cells were seeded in 96-well plates at a density of 1×10^4 cells per well and allowed to adhere for 24 h. Subsequently, the cells were treated with *m*-PPy (100 μL per well) and suspended in fresh culture medium for an additional 24 h. In the NIR irradiation group, C6 cells were co-cultured with *m*-PPy for 24 h and then exposed to an 808 nm laser. After irradiation, the cells were rinsed with PBS and incubated with 20 μL of MTT solution (5 mg mL^{-1}) for 4 h at 37 °C. The medium was discarded, and 150 μL of dimethyl sulfoxide (DMSO) was added to each well. The absorbance at 490 nm was measured using a microplate reader (BioTek Synergy H1). Live/dead cell staining was performed using calcein-AM/PI (Thermo Fisher Scientific). After treatment, the cells were incubated with PBS containing 2 μM of calcein-AM and 4 μM PI for 30 minutes. Following this, the cells were washed, and the morphology was observed under a laser scanning confocal microscope (Leica TCS SP8).

2.5 *In vitro* phototherapy

C6 glioma cells were seeded in 6-well plates at a density of 5×10^3 cells per well, and received different treatments: the control group (no treatment), irradiation group (808 nm laser, 0.3 W cm^{-2}, 10 min), and the *m*-PPy + irradiation group. After 10 min irradiation and 24 h incubation, several assays were conducted.[40] Total cellular protein was extracted using RIPA lysis buffer (Beyotime) containing a 1% protease inhibitor cocktail (Roche). Protein quantification was performed using the BCA method (Thermo Scientific), and 40 μg of total protein was subjected to SDS-PAGE (12% separating gel, 120 V for 90 min). Proteins were subsequently transferred onto PVDF membranes (Millipore, 0.45 μm) at 300 mA for 2 h and blocked with 5% skim milk in TBST for 1 h at room temperature. Membranes were incubated overnight at 4 °C with primary antibodies targeting Bax (1:1000, Abcam ab32503), Bcl-2 (1:800, CST #4223), and Cleaved Caspase-3 (1:500, CST #9664), followed by HRP-conjugated secondary antibodies (1:5000, CST) for 1 h at room temperature. Protein bands were visualized using an ECL chemiluminescence system (Bio-Rad ChemiDoc) and quantified using ImageJ software. RNA was extracted from cells using the TRIzol reagent (Invitrogen) and reverse transcribed into complementary DNA (cDNA) using a PrimeScript RT reagent kit (Takara). RT-qPCR was performed with SYBR Green Master Mix (Roche) on a QuantStudio 5 system (Applied Biosystems) to assess the expression levels of Bax, Bcl-2, and the reference gene GAPDH (primer sequences are provided in the supplementary materials). Relative gene expression was calculated using the $2^{-\Delta\Delta Ct}$ method. Apoptosis was analyzed by double-staining cells using the Annexin V-FITC/PI apoptosis detection kit (BD Biosciences). Flow cytometry (BD FACSCanto II) was employed to detect apoptotic populations, with 10 000 events recorded per sample. The early (Annexin V+/PI-) and late (Annexin V+/PI+) apoptosis rates were quantified using FlowJo V10 software. All experiments were conducted in triplicate, and data were expressed as mean ± standard deviation.

2.6 *In vivo* phototherapy

All animal experiments were performed in compliance with the relevant national and institutional guidelines, including the "Regulations for the Administration of Affairs Concerning Experimental Animals" of China, the guidelines of Harbin Medical University, and the ARRIVE 2.0 guidelines. The experimental procedures were approved by the Institutional Animal Care and Use Committee (IACUC) of Harbin Medical University (Approval Case Number: YJSDW2022-233).

A subcutaneous C6 glioma model in BALB/c nude mice (6–8 weeks old, female, 18–22 g) was established by subcutaneous injection of 5×10^6 C6 cells in 100 μL PBS. When tumors reached approximately 100 mm^3, mice were randomly divided into three groups ($n = 6$): Control group (no treatment), NIR group (irradiation only, 808 nm, 0.3 W cm^{-2}, 10 min), and *m*-PPy + NIR group (intratumoral implantation of *m*-PPy film followed by irradiation).[41] During the treatment, temperature changes of the tumor site were monitored in real time using a FLIR A65sc thermal imaging camera. Tumor volume changes were recorded on the 0^{th}, 3rd, 7th and 14th days post-treatment. The tumor volume was calculated as $V = 0.5 \times \text{length} \times \text{width}^2$. Additionally, body weight changes of the mice in each group were monitored every two days to assess systemic toxicity. At the end of the treatment, venous blood was collected *via* retro-orbital bleeding for blood analysis, including complete blood count (Mindray BC-2800Vet), liver and kidney function markers (Roche Cobas c311).

2.7 Integrated PTT-EEG monitoring system for *in vivo* glioma management

An integrated diagnosis and treatment system was developed on an *in situ* C6 glioma model in SD rats (200–250 g, female). The glioma model was established by stereotactic injection of 5×10^5 C6 cells into the right striatum (coordinates: 3 mm lateral, 1 mm anterior to bregma, depth 5 mm). This system features the precise attachment of *m*-PPy film to the surface of the brain tissue overlying the tumor region. The therapeutic process

employs an 808 nm laser (0.3 W cm^{-2}, 10 min) for PTT, while cortical electroencephalographic signals are simultaneously collected using a 32-channel Neuroscan system (sampling rate: 2000 Hz, bandpass filter: 0.1–100 Hz). To assess the reliability of the system, the following experimental approaches were employed: (1) The power spectral density of θ waves (4–8 Hz) and β waves (12–30 Hz) was compared before and after treatment using the EEGLAB toolbox in MATLAB. (2) Intraoperative neuromodulation scenarios were simulated using a microinjection pump (KD Scientific) for local administration of dopamine (10 μM, 2 μL) and dosulepin (2 mg kg^{-1}, 5 μL). (3) Quantitative tumor volume measurements were performed using MRI scans (T2-weighted sequences, TR/TE = 3000/80 ms, slice thickness 1 mm) on a 7T small animal MRI scanner (Bruker BioSpec) on the 1st, 3rd, 7th, and 14th days post-treatment. Immunohistochemical analysis was employed to evaluate the expression of Anxa5, Csrp3, and Septin-4 proteins in the tumor tissue (primary antibody dilution: 1:200, DAB chromogenic reaction) with a semi-quantitative analysis conducted using Image-Pro Plus software (Media Cybernetics) based on integrated optical density (IOD) measurements from five random fields per section.

At the same time, we used ZrC nanoparticles as a photothermal converter for PTT of intracranial glioma (injected intratumorally, 100 μL of 1 mg mL^{-1}), and finally compared it with the internal metal residues in the brain after PTT mediated by *m*-PPy, using Inductively Coupled Plasma-Mass Spectrometry (ICP-MS, Agilent 7900), following tissue digestion with 65% HNO_3 at 80 °C for 4 h. All tissue sections were stained with hematoxylin and eosin (H&E) and evaluated for inflammation by two independent pathologists under a double-blind protocol using a semi-quantitative scoring system (0–3 scale for inflammatory cell infiltration).

2.8 Statistical analysis

The experimental procedures were conducted with meticulous attention to detail, employing five replicates for each measurement. Quantitative data are presented as the mean ± standard deviation (SD). Statistical analysis was performed using Student's *t*-test to assess the significance of differences between experimental and control groups. Statistical significance was defined as $^{*}P < 0.05$, $^{**}P < 0.01$, and $^{***}P < 0.001$.

2.9 Characterizations

UV-Vis-NIR absorption spectra were acquired on a spectrophotometer (LAMBDA 1050 + spectrophotometer, PerkinElmer, USA). The crystalline phase of the samples was determined by X-ray diffraction (XRD) analysis conducted using an Empyrean instrument from Panalytical, Netherlands. High-resolution Scanning Electron Microscope (SEM) images were captured utilizing microscopy systems (FEI TALOS F200 and FEI 400FEG, USA). Visualization of stained cells was performed on a confocal laser scanning microscope (CLSM, Fluoview FV3000 OLYMPUS, USA). Surface modifications were characterized using Fourier Transform Infrared Spectroscopy (FTIR, Tensor 27, BRUKER, USA). Real-time monitoring of temperature was achieved utilizing an infrared camera system (FLIR System i7).

3 Results and discussion

3.1 Characterizations of *m*-PPy

Fig. 1a illustrates the fabrication of polypyrrole (PPy) films with engineered surface microstructures *via* electrochemical deposition using a templated patterning approach. The freestanding films exhibit uniform morphology with well-defined micropyramidal architectures confirmed by scanning electron microscopy (SEM) (Fig. 1b and c). Atomic force microscopy (AFM) revealed a significantly enhanced surface roughness (R_a = 298 ± 62 nm) compared to planar control films (Ra = 109 ± 45 nm) (Fig. S1, SI). The hierarchical micro-/nano-architecture enhanced light harvesting for photothermal conversion and improved bio-interface contact. By optimizing the electrodeposition parameters, we have successfully prepared flexible thin films with adjustable thickness (1–5 μm) and flexibility (Fig. S2, SI). Notably, sub-3 μm films demonstrated superior tissue conformability (contact angle <15° with ex vivo brain tissue) attributed to the reduced bending stiffness (0.8 ± 0.1 MPa elastic modulus), matching the mechanical compliance of cerebral parenchyma (1–5 kPa). The PPy film was characterized using XRD, FT-IR, XPS and Raman spectroscopy. The XRD pattern shows a diffractive peak at $2\theta = 25.6^{\circ}$, corresponding to the (020) crystal plane of PPy (Fig. 1d). The FT-IR spectrum exhibited characteristic peaks corresponding to C=C (1596 cm^{-1}) and C–N (1442 cm^{-1}) stretching vibrations, as well as C–H in-plane bending vibrations (1307 cm^{-1}), which are consistent with the standard characters of polypyrrole (Fig. 1e). The full-range XPS spectrum (Fig. 1f) indicates that the binding energy of the N 1s core level spectrum is 399.8 eV, corresponding to the secondary amine nitrogen (–NH–) structure in the pyrrole ring. The peaks at 284.6 eV and 286.2 eV in the C 1s spectrum correspond to C–C/C=C and C–N bonds, respectively. Additionally, the peak at 531.8 eV in the O 1 s spectrum can be attributed to adsorbed oxygen or surface oxidation species, such as C=O or –OH. The Raman spectrum (Fig. 1g) shows typical deformation vibration peaks at 935 cm^{-1} and 1050 cm^{-1}, while a strong peak at 1580 cm^{-1} corresponds to the C=C stretching vibration of the conjugated skeleton. Mechanical profiling demonstrated remarkable stretchability (13.16% fracture strain) and interfacial adhesion strength (20.3 ± 2.5 kPa shear adhesion, Fig. 1h and i), originating from van der Waals force amplification through micropyramidal contact points. This unique mechanical property enables dynamic adaptation to physiological micro-motions (≈200 μm amplitude from cardiopulmonary pulsations) while maintaining stable electrophysiological coupling.

3.2 Electrochemical and photothermal performances of PPy

First, we investigated the optimal pyrrole:PTSA molar ratio (Fig. 2a). A ratio of 2 : 1 yielded the highest conductivity (185 ± 12 S cm^{-1}) and excellent NIR absorption (800–1100 nm, Fig. 2b). Under 808 nm irradiation (0.3 W cm^{-2}, Fig. 2c), the film

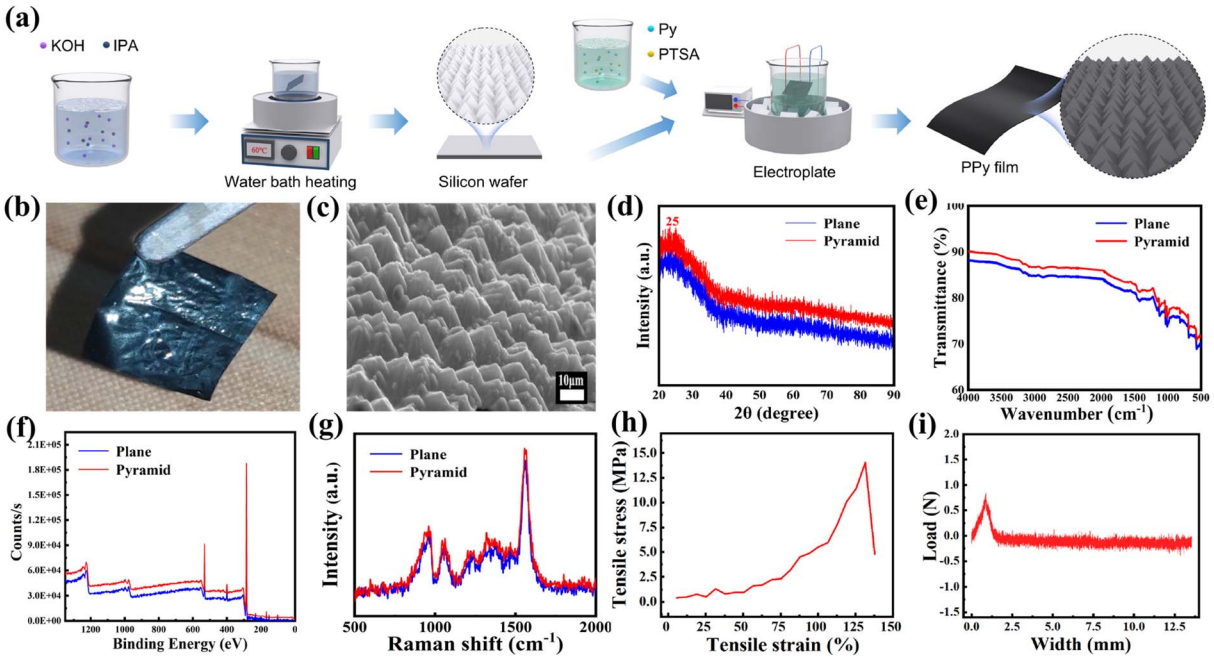

Fig. 1 (a) Schematic of the electrochemical fabrication process of *m*-PPy (Py : PTSA = 2 : 1). (b) Photograph of the freestanding *m*-PPy film. (c) SEM image of *m*-PPy. (d) XRD pattern, (e) FT-IR spectra, (f) XPS spectrum, (g) Raman spectrum, (h) Stress–strain curve, and (i) shear adhesion strength measurement of *m*-PPy.

demonstrated a rapid temperature elevation to 58.3 ± 1.5 °C within 120 s. It also exhibited an excellent cycling stability with >95% efficiency retention after 5 on/off cycles (Fig. 2d). The micropyramidal PPy showed a greater absorbance and photothermal effect than planar PPy. We think the enhanced performance of *m*-PPy films can be attributed to the synergistic interplay between the chemical structure and microarchitecture. The micropyramidal topography increases the effective surface area for light–matter interaction, promoting multiple internal reflections and thereby amplifying NIR absorption. This architectural feature facilitates efficient photothermal conversion by enhancing the excitation and relaxation of polaronic and bipolaronic states within the conjugated PPy backbone, a mechanism central to its photothermal efficiency[Ref]. Furthermore, the high aspect ratio of the pyramids reduces the interfacial charge transfer resistance, as evidenced by EIS, by providing a larger electrochemically active surface area (ECSA) and shorter diffusion pathways for ions. The

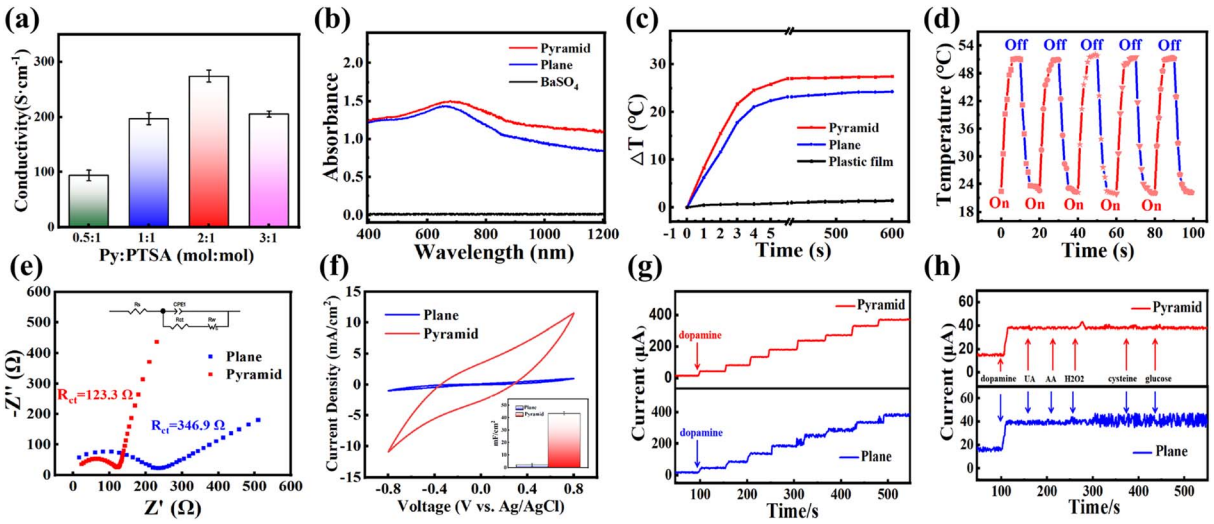

Fig. 2 (a) Electrical conductivity of films synthesized with varied molar ratios of pyrrole:PTSA. (b) UV-vis-NIR spectra. (c) Time-dependent photothermal heating profiles. (d) Cyclic stability of micropyramidal PPy. (e) Impedance test. (f) CV curves. Chronoamperometric assessment of (g) stability and (h) anti-interference.

optimized pyrrole:PTSA ratio of 2 : 1 was critical in achieving a balance between conjugation length and doping level, maximizing both electrical conductivity and NIR absorbance. These design considerations underscore that the functionality of *m*-PPy is not merely a consequence of material choice, but of deliberate chemical and structural engineering at the micro- and nano-scale. This work also studied the influence of power density (for laser irradiation) on the temperature elevation. A higher applied power resulted in a greater temperature elevation. Power-dependent temperature modulation (42–60 °C, Fig. S3, SI) enables precise thermal control for tumor ablation for preventing collateral neural damage (<42 °C safety threshold). Electrochemical impedance spectroscopy (EIS) (Fig. 2e) revealed a 64.5% reduction in interfacial impedance for micropyramidal PPy films (123.3 Ω) compared to their planar counterparts (346.9 Ω), being attributable to an enhanced electrochemically active surface area (ECSA) and optimized charge transport pathways enabled by the hierarchical architecture. Cyclic voltammetry (Fig. 2f) demonstrated the exceptional charge storage capacity of the micropyramidal PPy electrode, which achieved a specific capacitance of 43.36 mC cm^{-2} at 100 mV s^{-1}, being a 19.4-fold improvement over the planar PPy electrode (2.23 mC cm^{-2}). Chronoamperometric assessment in physiological media (Fig. 2g) showed a 131% enhanced dopamine sensitivity (ΔI = 1.32 μA μM^{-1} *vs.* 0.57 μA μM^{-1} for planar) with rapid signal recovery (<30 s baseline restoration, RSD <3.2%), while the selectivity (Fig. 2h) exhibited an 89.5% ± 4.3% signal suppression against interferents (glutamate ascorbic acid), benefitting from microstructure-mediated optimization of diffusion layer dynamics.

3.3 *In vitro* anti-cancer performance

The anti-tumor effect of *m*-PPy film was then evaluated *in vitro*. Under irradiation of 0.3 W cm^{-2}, the temperature at the material–tissue interface increased to 48.2 ± 0.7 °C within 10 min; tumor cells (>42 °C). It also showed the power dependence of the temperature increase. Cell viability assays (Fig. 3b and c) revealed that apoptosis of C6 glioma cells was significantly dependent on irradiation time/power density (***p < 0.001). A higher power density and extended duration led to higher temperatures and, consequently, increased cell apoptosis. Flow cytometry analysis (Fig. S4, SI) indicated that the apoptosis rate in the PPy + NIR group was considerably higher than that in the control group (early apoptosis: 14.58% ± 4.16% *vs.* the control group: 1.10% ± 1.12%), suggesting that early apoptosis is a primary mechanism of cell death under these photothermal conditions. Molecular mechanism studies (Fig. S5 and S6, SI) revealed that the observed photothermal therapy (PTT) effects were associated with transcriptional changes in genes linked to apoptotic pathways. Specifically, the expression of Annexin V (*Anxa5) increased threefold (*p < 0.0001), CSRP3 increased 2.1-fold (**p < 0.0001), and *Septin-4* expression decreased to 47% of that in the control group (*p < 0.001). Western blotting and qPCR results are consistent with the above results. The Calcein-AM/PI double staining experiment (Fig. 3d) showed that both the control group and the material-only group exhibited only

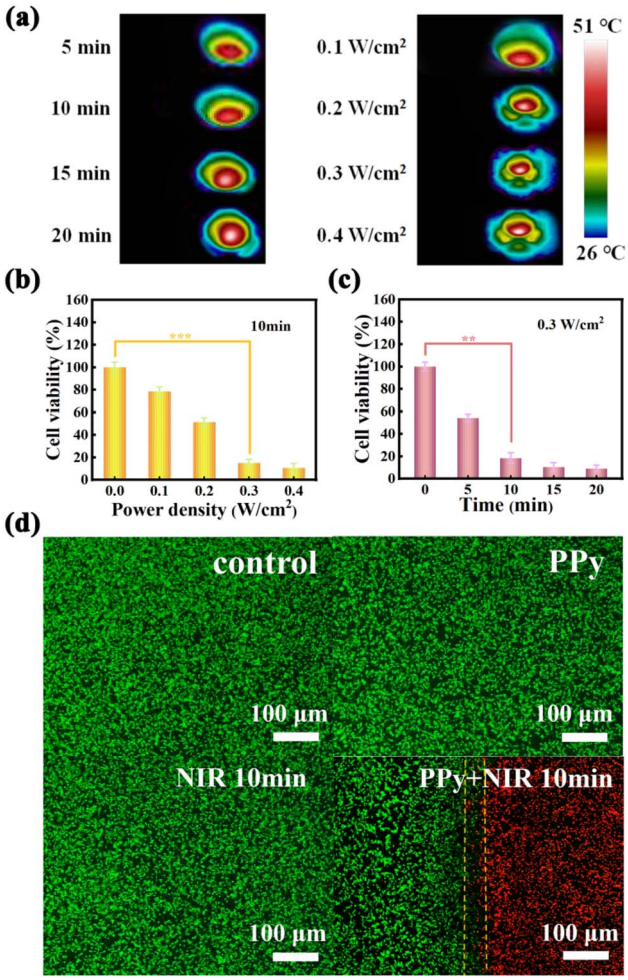

Fig. 3 (a) Time-temperature profiles under a 0.3 W cm^{-2} irradiation for different durations and varied powder densities for 10 min. (b and c) Dose-dependent cell viability (***p < 0.001). (d) Live/dead fluorescence images.

green fluorescence (survival rate >98%, manually counted under a fluorescence microscope), confirming that the material itself is non-toxic. Notably, NIR-only irradiation (5/10 minutes) did not cause significant cell death. When PPy was combined with 5 min irradiation, cell death exceeded 90% in the central material-covered region. The edge region exhibited a clear red-green fluorescence transition zone due to the thermal diffusion gradient (apoptosis rate 62.3% ± 5.8%). When the light exposure was extended to 10 min, the material-covered area (with a central temperature of 48.2 ± 0.5 °C) achieved complete ablation (apoptosis rate >99%), and the width of the edge transition zone decreased from 325 ± 45 μm to 93 ± 12 μm (***p < 0.001), demonstrating that precise control of the treatment boundary can be achieved by adjusting the irradiation parameters. High-magnification observations (Fig. S7, SI) further confirmed the clear boundary between the material-covered area and the unirradiated area, proving its precise spatial control.

3.4 *In vivo* anti-cancer properties

In this work, we firstly studied the antitumor performance of *m*-PPy film in subcutaneous transplantation tumor models in Balb/c nude mice (Fig. 4a). The *m*-PPy film patch was tagged on the tumor site. The *in vivo* photothermal conversion action was investigated with a thermal camera and the temperature changes were recorded (Fig. 4b and d). Under 808 nm laser irradiation (0.3 W cm^{-2}), the PPy + NIR group exhibited a higher temperature elevation at the tumor site ($\Delta T = 16.7$ °C) than that in the NIR-only control group ($\Delta T = 6.4$ °C). Nearly complete ablation of the tumor was observed in the PPy + NIR-treated group (98.7% volume reduction on day 14), while the control and NIR-only groups exhibited aggressive tumor progression (682% and 517% expansion, respectively) (Fig. 4c and e). During the treatment, all treated mice maintained normal behavior. Transient weight loss (7.2% maximum at 48 h post-treatment, Fig. 4f) was observed in the PPy + NIR groups on the first 3 days post treatment, potentially being attributable to photothermal stress-induced metabolic recalibration. Blood biochemistry (Fig. S8, SI) revealed that hepatic/renal function markers and hematological indices were within normal ranges, confirming the systemic biocompatibility. These findings suggest that PPy-mediated photothermal therapy achieves precision tumor eradication.

3.5 Bimodal functional validation of the integrated PTT-EEG monitoring system

This study addresses the current limitations in PTT research on gliomas, which predominantly relies on subcutaneous tumor models and lacks real-time intraoperative complication monitoring. Intraoperative EEG monitoring revealed sustained *δ*-wave dominance (>60%) during simulated hemorrhagic shock, consistent with clinical findings that delta power increases in tumor-affected cortical regions.[42] While photothermal therapy has shown promise in preclinical glioma studies, we have innovatively established an orthotopic C6 glioma model in SD rats and developed a synchronized EEG monitoring system and an M-shaped bioelectrode for signal collection. Gliomas are prone to rupturing when injected with nanoparticles. Hence, the *m*-PPy film patch can not only avoid particle residue, but also facilitate glioma treatment operation. As illustrated in Fig. 5a, the orthotopic tumor model was successfully constructed *via* surgical operation. Preoperative EEG recordings using the *m*-PPy film (Fig. 5b) demonstrated a stable record of *α*-waves (8–13 Hz) under normal anesthesia, with a power spectral density of 98.7 ± 3.2 μV^2 Hz^{-1} and a signal-to-noise ratio (SNR) of >35 dB, confirming the excellent electrophysiological signal. M-PPy electrodes were used for simultaneous temperature regulation and electrophysiological signal detection during intraoperative monitoring (Fig. 5c).

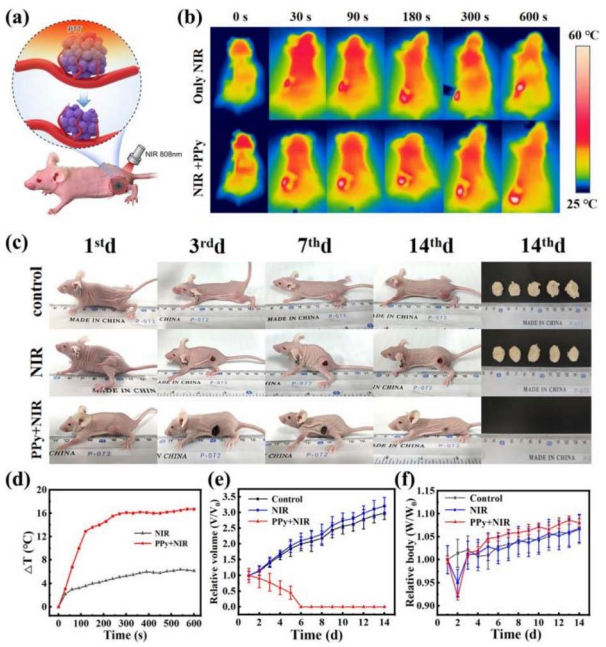

Fig. 4 (a) Subcutaneous glioma treatment protocol for tumor-bearing Balb/c nude mice. (b) Infrared thermograms of tumors; (c) macroscopic tumor progression images; (d) real-time temperature of tumor; quantitative curves of (e) relative tumor volume and (f) body weight.

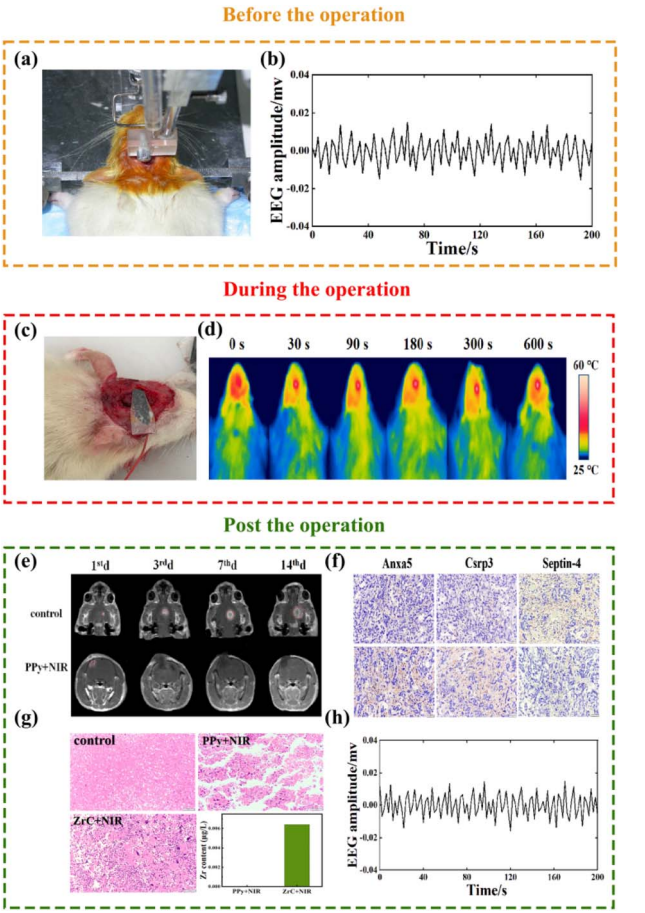

Fig. 5 Before the operation: (a) establishment of the orthotopic C6 glioma model in SD rats and (b) EEG recording under normal anesthesia using *m*-PPy film. During the operation: (c) photograph of the PTT-EEG monitoring system and (d) infrared thermal imaging during PTT. Post the operation: (e) MRI evaluation; (f) immunohistochemical analysis; (g) histological and ICP-MS analysis of metal residues; and (h) postoperative EEG monitoring.

Thermography (Fig. 5d) revealed that the *m*-PPy films precisely elevated the tumor temperature to 52.4 ± 1.2 °C (ΔT = 17.6 ± 1.3 °C) under 808 nm irradiation (0.3 W cm^{-2}), with a temperature gradient control accuracy of ±0.8 °C mm^{-1}. To investigate the availability of the EEG monitoring system, we recorded four typical intraoperative states during photothermal treatment by pharmacological interventions. (1) In the normal state, α-wave dominance was maintained (Fig. S9a). (2) A hypertensive state by dopamine surge triggered *a* >40% abrupt increase in γ-band power spectral density (Fig. S9b). (3) Respiratory excitation (Fig. S9c) induced characteristic *θ*-wave rhythm disruption. (4) Hemorrhagic shock (Fig. S9d) resulted in sustained *δ*-wave dominance (>60%) and *β*-wave suppression.[43,44] The EEG frequency changes are influenced by multiple physiological factors, and these associations should be interpreted as correlative rather than causative. Further studies with larger sample sizes and controlled interventions are needed to validate these preliminary observations. However, this work can help doctors better understand the real-time situations of patients during surgery and facilitate the handling of emergencies to a certain degree, which is particularly important for neurosurgery. Postoperative MRI evaluation (Fig. 5e) showed that the tumors in the treatment group were completely ablated since day 3, and the surrounding edema zone disappeared after 14 days. In contrast, the control group exhibited tumor volume expansion to 273.06% ± 98.87% of the initial size (Fig. S10, SI).

The treatment group also demonstrated steady body weight gain over 14 days (Fig. S11, SI), indicating good survival quality. Immunohistochemical analysis (Fig. 5f) indicated upregulated Anxa5 and Csrp3 expression, and downregulated Septin-4 in the treatment group, consistent with *in vitro* apoptosis results. The *m*-PPy-mediated therapeutic system of this work also exhibited unique advantages of no intracranial metal residue, as evidenced by H&E staining and ICP-MS results, resolving the long-term biosafety concerns associated with conventional metal electrodes (Fig. 5g). Postoperative EEG monitoring (Fig. 5h) revealed *a* <5% change in the *θ*/*β*-wave ratio, and the α-wave power is comparable to preoperative levels, proving the negligible impact on neural electrophysiological activity. By synergizing therapeutic and monitoring innovations, this study provides a novel solution for the precise PTT treatment of brain tumors.

To contextualize the performance of our *m*-PPy integrated system, we compared it with recently reported photothermal neural interfaces. Kim *et al.* developed a transparent ultrathin gold film system capable of simultaneous photothermal stimulation and neural signal recording, achieving precise temperature control at the neuronal interface.[45] While this system offers high-resolution temperature sensing, its primary focus is on neuromodulation rather than therapeutic tumor ablation. In contrast, our *m*-PPy system is specifically designed for glioma treatment, integrating complete tumor ablation with intraoperative EEG monitoring. Critically, unlike nanoparticle-based photothermal systems that face challenges related to long-term intracranial retention and biocompatibility, our freestanding film can be completely removed post-surgery, addressing a key clinical bottleneck in photothermal therapy translation.[46]

Furthermore, our EEG monitoring results align with clinical intraoperative electrocorticography findings, where tumor-affected cortical regions exhibit increased delta power and suppression of other frequency bands.[41] By integrating this clinically validated spectral analysis with real-time photothermal therapy, our system offers a unique platform for both treatment and intraoperative safety monitoring, a combination that is not present in the existing neural interface or photothermal therapy systems.

3.6 Proteomic analysis

Proteins serve as crucial executors of biological functions and play pivotal roles in regulating biological processes. Proteomic analysis was carried out in this work. Three biological replicates were collected for each treatment (Fig. 6a). Differential scatter plot analysis revealed 7007 significantly altered proteins,

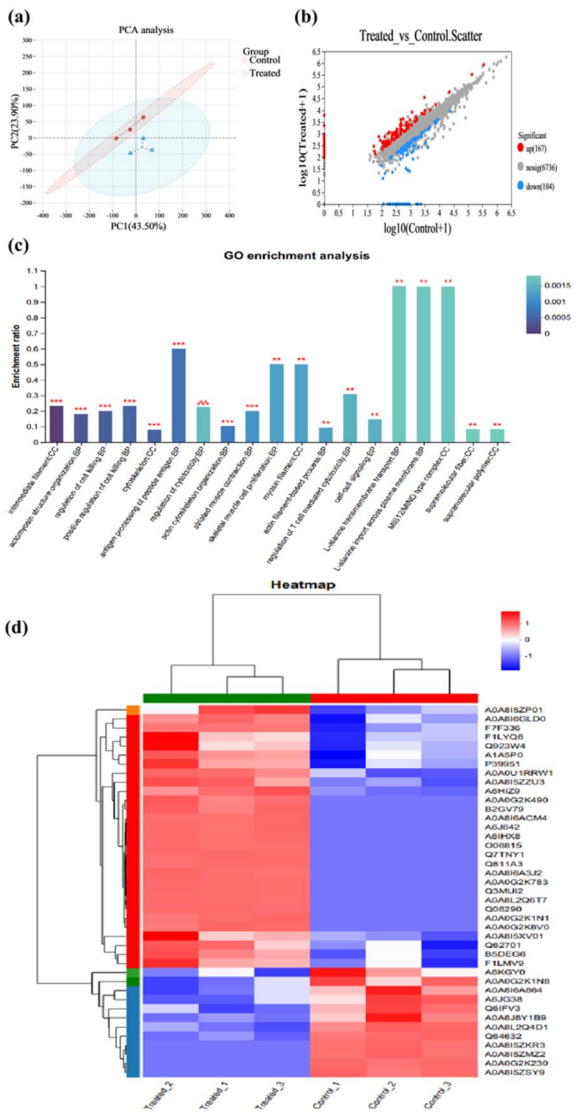

Fig. 6 Histoproteomic analysis of glioma. (a) PCA analysis; (b) differential protein scatter plot; (c) GO enrichment analysis of all differential proteins; and (d) heat maps of differential proteins associated with cell structure.

including 167 upregulated and 155 downregulated proteins (|fold change|≥2), indicating extensive biological changes induced by PTT treatment (Fig. 6b). Subsequently, functional and pathway enrichment analyses were conducted on the identified differential proteins. Gene Ontology (GO) analysis of SD rat gliomas after PTT treatment revealed significant enrichment of proteins involved in biological processes and molecular functions related to cell structure, cell death regulation, and immune responses (Fig. 6c). Kyoto Encyclopedia of Genes and Genomes (KEGG) pathway enrichment analysis of the differential proteins revealed several major pathways, including cell adhesion molecules, chemical carcinogenesis and reactive oxygen species pathways, calcium signaling pathway, motor proteins, and thermogenesis (Fig. S12, SI). Pathway analysis suggested that PPy-mediated PTT potentially modulated multiple biological processes and signaling pathways, thereby influencing both tumor cell behaviors and immune system activation. In the thermogenesis pathway, significant downregulation of NADH-ubiquinone oxidoreductase chain 2 and chain 4 (NDUFB2 and NDUFB4) post PTT treatment implied the inhibition of mitochondrial complex I function during treatment. Additionally, AMPK β2 subunit (Prkab2) was also downregulated post-treatment, potentially reflecting cellular adaptive responses to energy metabolism (Fig. S13, SI). KEGG pathway analysis of motor proteins revealed significant downregulation of several critical proteins, including actin-like proteins, myosins, and dyneins, underscoring their roles in cell motility, maintenance of cellular framework and intracellular substance transport (Fig. S14, SI). Hence, our findings provide new insights into the regulation of thermogenesis and motor protein pathways by PPy-mediated PTT treatment, which potentially alters tumor cell migration ability and cytoskeletal structure, thereby influencing their invasiveness and metastatic properties.

Next, we focused on proteins associated with cell structure to better understand how PPy-mediated PTT induces cell death by affecting tumor cell migration ability and cytoskeletal structure. Protein heat map analysis revealed a total of 41 differentially expressed proteins, with 29 upregulated and 12 downregulated proteins (Fig. 6d). Functional analysis based on Gene Ontology (GO) showed significant enrichment of these 41 differentially expressed proteins in cellular skeleton organization and regulation, intercellular interactions and cellular functional regulation (Fig. S15, SI)). These findings have deepened our understanding of the molecular mechanisms through which PPy-mediated PTT impacts the cellular skeleton and structure, providing theoretical support and guidance for its application in tumor treatment and tissue repair. Additionally, we examined proteins related to immune function to better understand how PPy-mediated PTT promotes anti-tumor immune responses. We identified 23 differentially expressed proteins, including 13 upregulated and 10 downregulated proteins (Fig. S16, SI). Pathway analysis based on Gene Ontology (GO) processes revealed significant enrichment of these 23 differentially expressed proteins in immune processes, particularly in immune response regulation, cell death regulation, and adaptive immune regulation, indicating the activation of specific immune pathways related to anti-tumor responses post PTT treatment (Fig. S17, SI).

4 Conclusions

This study successfully developed an integrated PTT-EEG monitoring system based on micro-pyramid-structured PPy films, offering a highly efficient, precise, and safe solution for glioma treatment. The experimental results confirmed that PPy films exhibit excellent photothermal conversion performance and electrochemical characteristics. The biomimetic microstructure not only enhanced tissue interface compatibility but also optimized charge transport efficiency. *In vitro* and *in vivo* experiments have suggested that this method effectively ablates tumors through heat-induced apoptosis and mitochondrial dysfunction, leading to complete tumor clearance. Crucially, the integrated PTT/EEG system can capture real-time neuroelectrophysiological changes during surgery with a temperature control accuracy of ±0.8 °C. Importantly, this approach avoids the long-term retention risk associated with traditional metal materials. Proteomics analysis revealed that PTT inhibited tumor migration and activated anti-tumor immunity by regulating actin and immune-related pathways.

Author contributions

Haoyang Zhang: writing – original draft, visualization, software. Ke Shi: data curation, formal analysis. Wenxuan Zhang: investigation, methodology. Xue Chen: writing. Xi Wang: writing. Yan Zhao: project administration. Hengyuan Pang: validation. Xi Chen: writing – review & editing. Jianjiao Wang: writing – review & editing, formal analysis, conceptualization.

Conflicts of interest

There are no conflicts to declare.

Data availability

The data that support the findings of this study are available from the corresponding author upon reasonable request.

Supplementary information (SI): detailed experimental procedures, characterization of materials, additional photothermal performance data, EEG signal processing methods, and figures (Fig. S1–S11). See DOI: https://doi.org/10.1039/d6ra00499g.

Acknowledgements

This work was funded by the Lateral Project of Harbin Medical University (No. 22992240095 and 8207101369).

Notes and references

1 H. C. Tsai, P. Y. Liu, Z. J. Tong, C. Y. Wu, Y. R. Lin, K. C. Wei, C. Y. Huang, K. T. Chen, Y. J. Lin, P. Y. Chen and H. T. Wang,

Mol. Cancer Ther., 2025, DOI: 10.1158/1535-7163.Mct-25-0117.
2 S. M. Watson, E. P. Harvey, N. Pishesha, H. L. Ploegh and T. A. Springer, *J. Biol. Chem.*, 2025, 110374.
3 R. Wei, J. Zhou, B. Bui and X. Liu, *BMC Cancer*, 2024, **24**, 974.
4 J. Haemmerli, S. Khatchatourov, E. Chaboudez, L. Roth, A. Sandralegar, I. Janssen, D. Migliorini, K. Schaller and P. Bijlenga, *Front. Oncol.*, 2025, **15**, 1551937.
5 J. Wach, M. Vychopen, A. E. Basaran, A. Güresir, C. Seidel, A. Kühnapfel and E. Güresir, *J. Neurosurg.*, 2025, **142**, 1319–1330.
6 K. Sadowski, A. Jażdżewska, J. Kozłowski, A. Zacny, T. Lorenc and W. Olejarz, *Int. J. Mol. Sci.*, 2024, **25**, 5774.
7 J. Li, Y. Sun, X. Zhao, Y. Ma, Y. Xie, S. Liu, B. Hui, X. Shi, X. Sun and X. Zhang, *Cell Death Dis.*, 2023, **14**, 259.
8 M. Li, L. Lu, Q. Bao, M. Zhou, B. Nie, Y. Liu, K. Shu, T. Lei and M. Zhu, *J. Nanobiotechnology*, 2025, **23**, 239.
9 Q. Yue, Z. Wang, Y. Shen, Y. Lan, X. Zhong, X. Luo, T. Yang, M. Zhang, B. Zuo, T. Zeng, J. Lu, Y. Wang, B. Liu and H. Guo, *Adv. Sci.*, 2024, **11**, e2309290.
10 M. Jezierzański, N. Nafalska, M. Stopyra, T. Furgoł, M. Miciak, J. Kabut and I. Gisterek-Grocholska, *Curr. Oncol.*, 2024, **31**, 3994–4002.
11 S. D. Lustig, S. K. Kodali, S. L. Longo, S. Kundu and M. S. Viapiano, *Anticancer Res.*, 2022, **42**, 723–730.
12 F. Yasinjan, Y. Xing, H. Geng, R. Guo, L. Yang, Z. Liu and H. Wang, *Front. Immunol.*, 2023, **14**, 1255611.
13 J. Gallo and A. Villasante, *Int. J. Mol. Sci.*, 2023, **24**, 15486.
14 J. Domingo-Diez, L. Souiade, V. Manzaneda-González, M. Sánchez-Díez, D. Megias, A. Guerrero-Martínez, C. Ramírez-Castillejo, J. Serrano-Olmedo and M. Ramos-Gómez, *Int. J. Mol. Sci.*, 2023, **24**, 15933.
15 W. Zhang, K. Cai, Z. Sun, Q. Xiang, L. Yuan, M. Fu, X. Liu, M. F. F. Foda, Z. Ye, J. Huang, H. Liu, H. Han, H. Liang, H. Dong and X. Zhang, *ACS Nano*, 2023, **17**, 18932–18941.
16 Q. Zhang, E. Li, Y. Zhang, Y. Chen, D. Wang and S. Wang, *ACS Biomater. Sci. Eng.*, 2024, **10**, 6210–6217.
17 L. Zhang, W. Chen, L. Cheng, L. Jiang, X. Deng, J. Yan and H. Yang, *J. Mater. Sci.: Mater. Electron.*, 2021, **32**, 5176–5185.
18 A. Mizera, P. Ławniczak, A. T. Dubis, K. H. Markiewicz and A. Łapiński, *ChemPhysChem*, 2025, **26**, e202401151.
19 W. Liu, S. Ji, J. i Zhao, M. Qin and H. Dai, *Surf. Interf.*, 2026, **80**, 108179.
20 H. Zhao, C. Li, X. Shi, J. Zhang, X. Jia, Z. Hu, Y. Gao and J. Tian, *EBioMedicine*, 2024, **106**, 105243.
21 K. Yang, H. Xu, L. Cheng, C. Sun, J. Wang and Z. Liu, *Adv. Mater.*, 2013, **25**, 945.
22 H. Yamaguchi, M. Okada, T. Otani, J. On, S. Shibuma, T. Takino, J. Watanabe, Y. Tsukamoto, R. Ogura, M. Oishi, T. Suzuki, A. Ishikawa, H. Sakata and M. Natsumeda, *Pharmaceuticals*, 2025, **18**, 751.
23 K. J. Sweeney, M. Amoo, R. Kilbride, G. I. Jallo and M. Javadpour, *J. Neurosurg.*, 2024, **38**, 746–751.
24 P. Shen, S. Fleming, C. Westcott and V. Challa, *J. Surg. Oncol.*, 2003, **83**, 36–41.
25 H. Zhu, Z. Zhang, R. Jiang, L. Xu, X. Yang, J. Chen, Z. Wang, X. Xu and Z. Liu, *J. Nanobiotechnol.*, 2025, **23**, 203.
26 B. S. Dash, Y. J. Lu and J. P. Chen, *ACS Appl. Mater. Inter.*, 2024, **16**, 13543–13562.
27 D. Kawauchi and Y. Narita, *Int. J Clin. Oncol.*, 2025, **30**, 1276–1286.
28 J. Chen, Y. Gao, J. Zhong, X. Wu, Z. Leng, M. Liu, Y. Wang, Y. Wang, X. Yang, N. Huang, F. Xiao, M. Zhang, X. Liu and N. Zhang, *Cell Rep. Med.*, 2024, **5**, 101806.
29 I. L. Granerud, M. L. Fabritius, H. R. Jensen, K. Møller and M. K. Sørensen, *Acta Neurochir.*, 2025, **167**, 62.
30 S. B. Aboeleneen, M. A. Scully, G. C. Kramarenko and E. S. Day, *Int. J. Hyperther.*, 2023, **40**, 2272066.
31 B. Hasannejad-Asl, F. Pooresmaeil, E. Choupani, M. Dabiri, A. Behmardi, M. Fadaie, M. Fathi, S. A. Moosavi, S. Takamoli, E. Hemati, V. Y. Naei and F. Kazemi-Lomedasht, *CNS Neurol. Disord.: Drug Targets*, 2023, **22**, 18–26.
32 S. Mehrdadi, *Adv. Pharm. Bull.*, 2023, **13**, 512–520.
33 R. Dhapola, S. K. Beura, P. Sharma, S. K. Singh and D. HariKrishnaReddy, *Mol. Biol. Rep.*, 2024, **51**, 48.
34 D. Qi, Z. Liu, Y. Liu, Y. Jiang, W. R. Leow, M. Pal, S. Pan, H. Yang, Y. Wang, X. Zhang, J. Yu, B. Li, Z. Yu, W. Wang and X. Chen, *Adv. Mater.*, 2017, **29**, 1702800.
35 Q. Zhao, M. Zhu, G. Tian, C. Liang, Z. Liu, J. Huang, Q. Y. Yu, S. Tang, J. Chen, X. Zhao, Q. Zeng, C. Guo and D. Qi, *Adv. Healthcare Mater.*, 2023, **12**, 2203344.
36 X. Wu, Y. Ye, M. Sun, Y. Mei, B. Ji, M. Wang and E. Song, *Cyborg. Bionic. Syst.*, 2025, **6**, 0192.
37 Y. Xie, Y. Peng, J. Guo, M. Liu, B. Zhang, L. Yin, H. Ding and X. Sheng, *Fundam. Res.*, 2025, **5**, 17–28.
38 Y. Xia, Y. Liu, X. Hu, F. Zhao and B. Zeng, *ACS Sens.*, 2022, **7**, 3077–3084.
39 W. Zhou, H. Guan, K. Sun, Y. Xing and J. Zhang, *ACS Appl. Bio Mater.*, 2019, **2**, 2708–2714.
40 M. Tsol, Y. Chen, A. Gopalakrishnan, C. Ung, A. Khan, D. Upton and D. S. Ziegler, *J. Vis. Exp.*, 2025, **219**, e67349.
41 B. Díaz-Fernández, D. Henao-Herreno, J. Nieto, A. Evstratova, S. Cases-Cunillera, L. Deboeuf, A. Roux, E. Dezamis, M. Zanello, B. Mathon, C. Karachi, A. Carpentier, P. Varlet, J. Pallud, L. Capelle, C. Alvarado-Rojas, M. Le Van Quyen and G. Huberfeld, *Neuro. Oncol.*, 2025, **27**, 1758–1771.
42 C. Li, H. Xu, X. Cheng, X. Yu, Z. Gong, Y. He, L. Zhao and Z. Wang, *Chem.Eng. J.*, 2025, **526**, 170857.
43 E. Manquat, F. Vallée, E. Gayat, D. Sabbagh, M. Berto-Strouc, J. Joachim, J. Cartailler and A. Gramfort, *Anaesth. Crit. Care Pain Med.*, 2026, **45**, 101636.
44 C. Papageorgiou, E. Manios, E. Tsaltas, E. Koroboki, M. Alevizaki, E. Angelopoulos, M. Dimopoulos, C. Papageorgiou and N. Zakopoulos, *Int. J. Hypertens.*, 2017, 7247514.
45 D. Kim, J. W. Lee, S. Kang, W. Hong, J. Lee, H. J. Kwon, J. E. Jang, L. P. Lee and H. Kang, *Adv. Sci.*, 2025, **12**, e2411725.
46 T. Zeng, Y. Wang, Y. Zhang, Y. Bai, S. Lin, T. Zhu, Y. Zhou, W. Pan, P. Liu and J. Yang, *Adv. NanoBiomed. Res.*, 2026, e202500287.